Available online at www.sciencedirect.com
SCIENCE DIRECT
Journal of Inorganic Biochemistry 100 (2006) 786–800
Journal of Inorganic Biochemistry
www.elsevier.com/locate/jinorgbio

Characterization of synthetic oxomanganese complexes and the inorganic core of the O_2-evolving complex in photosystem II: Evaluation of the DFT/B3LYP level of theory

Eduardo M. Sproviero, Jose A. Gascon, James P. McEvoy, Gary W. Brudvig, Victor S. Batista *

Department of Chemistry, Yale University, 225 Prospect Street, P.O. Box 208107, New Haven, CT 06520-8107, United States

Received 7 December 2005; received in revised form 8 January 2006; accepted 9 January 2006
Available online 28 February 2006

Abstract

The capabilities and limitations of the Becke-3–Lee–Yang–Parr (B3LYP) hybrid density functional are investigated as applied to studies of mixed-valent multinuclear oxomanganese complexes. Benchmark calculations involve the analysis of structural, electronic and magnetic properties of di-, tri- and tetra-nuclear Mn complexes, previously characterized both chemically and spectroscopically, including the di-μ-oxo bridged dimers $[Mn^{III}Mn^{IV}(\mu\text{-}O)_2(H_2O)_2(terpy)_2]^{3+}$ (terpy = 2,2′:6,2″-terpyridine) and $[Mn^{III}Mn^{IV}(\mu\text{-}O)_2(phen)_4]^{3+}$ (phen = 1,10-phenanthroline), the Mn trimer $[Mn_3O_4(bpy)_4(H_2O)_2]^{4+}$ (bpy = 2,2′-bipyridine), and the tetramer $[Mn_4O_4L_6]^{+}$ with $L = Ph_2PO_2^-$. Furthermore, the density functional theory (DFT) B3LYP level is applied to analyze the hydrated Mn_3O_4CaMn cluster completely ligated by water, OH^-, Cl^-, carboxylate and imidazole ligands, analogous to the '3+1 Mn tetramer' of the oxygen-evolving complex of photosystem II. It is found that DFT/B3LYP predicts structural and electronic properties of oxomanganese complexes in pre-selected spin-electronic states in very good agreement with X-ray and magnetic experimental data, even when applied in conjunction with rather modest basis sets. However, it is conjectured that the energetics of low-lying spin-states is beyond the capabilities of the DFT/B3LYP level, constituting a limitation to mechanistic studies of multinuclear oxomanganese complexes where until now the performance of DFT/B3LYP has raised little concern.

Keywords: DFT/B3LYP; Photosystem II; O_2-evolving complex; Oxomanganese complex; Exchange coupling

1. Introduction

High-valent multinuclear oxomanganese complexes have been extensively investigated both experimentally [1–10] and theoretically [11–24], due to their central role in catalytic water-splitting. In particular, structural rearrangements in multinuclear oxomanganese model complexes have been studied at the density functional theory (DFT) level, implemented in conjunction with hybrid density functionals (e.g., the Becke-3–Lee–Yang–Parr (B3LYP) functional) [11–24], a computational approach that has been identified as the most successful methodology in an overwhelming number of investigations in many areas of chemical research. However, the quantitative capabilities and limitations of DFT, as applied to oxomanganese complexes, remain poorly understood. This paper explores the predictive power of DFT as applied to the description of synthetic oxomanganese complexes that have been thoroughly characterized both chemically and spectroscopically, with emphasis on the analysis of electronic and structural properties at the DFT/B3LYP level of theory [25,26]. Subsequently, the DFT/B3LYP methodology is applied to the analysis of an oxomanganese model complex that mimics the inorganic core of the oxygen evolving complex (OEC) of photosystem II (PSII) [27],

* Corresponding author. Fax: +1 203 432 6144.
E-mail address: victor.batista@yale.edu (V.S. Batista).

0162-0134/$ - see front matter © 2006 Elsevier Inc. All rights reserved.
doi:10.1016/j.jinorgbio.2006.01.017

the natural catalyst responsible for photosynthetic water-splitting in the thylakoid membranes of cyanobacteria and green-plant chloroplasts [28,29].

Previous theoretical studies have found that the DFT/B3LYP methodology typically overestimates Mn–Mn distances in model complexes with μ-oxo bridges, as compared to X-ray data, with typical errors in the 0.10–0.15 Å range [17,18]. Even more critical is the observation that B3LYP overestimates Mn–ligand distances along the Jahn–Teller axis of Mn^{3+} by as much as ~0.23 Å [17,18]. These problems seem to be rather serious, since they are comparable to typical structural rearrangements due to oxidation/reduction of the constituent ions (i.e., changes of Mn–ligand bond-lengths in the 0.1–0.2 Å range). In addition, it is known that hybrid functionals overestimate the relative stability of high-spin over low-spin states of transition metal complexes [30,31], a difficulty that can be critical in the process of identifying the nature of the ground electronic state, or in studies of spin-crossover phenomena in transition metal complexes [32–39]. Studies of well-characterized complexes are therefore essential to investigate the quantitative limitations of hybrid density functionals as applied to model open-shell transition metal compounds.

It is important to note that significant effort has been invested in the development of new functionals as well as in the re-parameterization of existing ones, although exact functionals have yet to be discovered [40]. Systematic benchmarks, typically including only main-group compounds, indicate net-incremental improvements, although significant breakthroughs have not been reported [41–61]. High-level benchmarks on open-shell transition metal species are much less frequently reported [39]. However, the study of transition metal compounds has been dominated by the well-established BP86 and B3LYP functionals [30,31,35,62–80], even when the parameterization of such functionals has not included any transition metal compound in the reference data set. Therefore, considering that the electronic structure of transition metal complexes and main group compounds are qualitatively different, it would not be surprising if these functionals were to exhibit important shortcomings in the description of low-lying spin states of open-shell transition-metal complexes [80–85]. It is thus essential to document the capabilities and limitations of these, otherwise successful, DFT methodologies in order to establish their range of validity and stimulate the development of more reliable functionals for transition metal compounds.

The present study is further motivated by several recent proposals to improve the performance of hybrid density functionals as applied to transition metal compounds by adjusting the amount of exact exchange admixture [31,35,39,86]. Of particular interest is the analysis of whether such adjustments are necessary to improve the ability of the method to describe structural and electronic properties of oxomanganese complexes, including Mn–Mn distances characterized by X-ray studies and exchange coupling constants probed by electron paramagnetic resonance (EPR) experiments. These studies are expected to be particularly relevant to mechanistic studies of the photo-catalytic water-oxidation reaction at the OEC of PSII. X-ray spectroscopic measurements reveal changes of about 0.1–0.2 Å in the Mn–Mn distances of the OEC, induced by its oxidation/reduction during the catalytic cycle [87,88]. Computational studies of these redox-linked structural changes thus represent important computational challenges, which require the validation of DFT methods as applied to well-characterized oxomanganese complexes, including the dark-stable S_1 state of the OEC.

Several synthetic oxo-manganese complexes have been studied by EPR and X-ray spectroscopy in prolonged and systematic studies to gain fundamental understanding of the process of O_2 evolution [1]. The calculations reported in this paper include four of these synthetic Mn-oxo complexes [2,4,5,89], including the di-μ-oxo $Mn^{III}Mn^{IV}$ complexes $[Mn^{III}Mn^{IV}(\mu\text{-}O)_2(H_2O)_2(terpy)_2]^{3+}$ (terpy = 2,2′:6,2″-terpyridine) and $[Mn^{III}Mn^{IV}(\mu\text{-}O)_2(phen)_4]^{3+}$ (phen = 1,10-phenanthroline), the $[Mn_3O_4(bpy)_4(H_2O)_2]^{4+}$ (bpy = 2,2′-bipyridine) trimer, and the $[Mn_4O_4L_6]^{+}$ tetramer, with $L = Ph_2PO_2^-$. Having documented the capabilities and limitations of the DFT methodology, as applied to these four benchmark complexes, further calculations are carried out to characterize the structural stability of the cuboidal $[Mn_3CaO_4Mn]^{8+}$ cluster ion completely ligated with water, OH^- and Cl^-, a structure based on the inorganic core of the OEC modeled in the recent X-ray crystal structure of PSII obtained by Ferreira et al. [27].

The paper is organized as follows. Section 2 describes the computational methods and the preparation of the model systems. Results are presented and discussed in Section 3. The structural analysis of benchmark oxomanganese complexes is presented in Section 3.1.1 as compared to X-ray experiments. Computations of exchange coupling constants of oxomanganese benchmark complexes are reported in Section 3.1.2. Section 3.3 presents computations of biomimetic model complexes with a cuboidal Mn_3CaO_4Mn cluster, completely ligated with water, OH^- and Cl^- and model ligands that mimic the environment of the OEC. Section 4 summarizes and concludes.

2. Methods

2.1. Molecular models

The X-ray atomic coordinates of the Mn complexes were obtained from the Cambridge Crystallographic Data Center (CCDC) with reference codes FIQFIU [2], YEMCIC [4], JEWNII [5], and HIRDIV [89]. All ab initio computations were performed at the DFT/B3LYP level of theory by using the programs Jaguar 5.5 [90] and Gaussian 03 [91]. A combination of basis sets has been implemented in order to perform efficient, yet accurate,

calculations. Such a combination of basis sets includes the LACVP basis set, which is necessary to consider non-relativistic electron core potentials (ECPs) for the Mn ions, the 6-31G(d) and 6-31G(2df) basis sets for bridging O^{2-} ions in order to include polarization functions associated with μ-oxo species, and the 6-31G/3-21G basis set for the rest of the atoms. Accurate calculations of exchange coupling constants, however, required the TZV basis set [92,93].

Fully optimized molecular structures were obtained through minimum-energy geometry optimizations at the DFT/B3LYP(LACVP,6-31G(2df),6-31G(d),6-31G,3-21G) in a broken symmetry (BS) state. In this state the α and β densities are allowed to localize on different atomic centers, providing a multiconfigurational character to the spin-state. Calculations of electronic and structural properties of the fully relaxed structures allow direct comparisons with experimental measurements, including the analysis of geometrical parameters such as bond lengths, bond angles and dihedral angles, and electronic properties such as spin populations, exchange coupling constants and electrostatic potential (ESP) atomic charges. Ionic spin states were characterized according to the analysis of Mulliken atomic spin density populations.

Preparation of the models was subject to the constraints of total charge and total spin multiplicity, consistent with experimental data. Different arrangements of individual spin states were analyzed (subject to the constraints of total charge and spin multiplicity) by relaxing the molecular structures from appropriate initial-guess spin-electronic states, based on ligand field theory [94]. Direct comparisons with both experimental magnetic and X-ray diffraction data allow one to evaluate the capabilities of the DFT/B3LYP methodology with regards to both electronic and structural properties, beyond the *minimum energy* criteria. Furthermore, the comparative analysis of both complete molecular structures and simplified models allows one to evaluate the capabilities and limitations of simplified model systems that might significantly reduce the computational cost of the calculations, and the effect of large and bulky substituents on the minimum energy geometries of the complexes.

2.2. Exchange coupling constants

Calculations of exchange coupling constants were based on the BS approach, a methodology that has already been applied in conjunction with density functional theory methods to studies of other metal clusters [19,20,95–98].

The exchange coupling constants J_{ij} between centers i, j associated with the Heisenberg Hamiltonian

$$\hat{H} = -\sum_{i,j}^{N} J_{ij}\hat{S}_i \cdot \hat{S}_j \tag{1}$$

are defined according to the BS approach as follows:

$$J_{ij} = \frac{E_{\mathrm{BS}}^{(ij)} - E_{\mathrm{HS}}^{(ij)}}{2S_iS_j + \min(S_i, S_j)}, \tag{2}$$

where S_i is the spin corresponding to metal center i and $E_{\mathrm{BS}}^{(ij)}$, $E_{\mathrm{HS}}^{(ij)}$ correspond to the magnetic energy contributions from the pair of metal centers i and j, assuming weak coupling with $S_i < S_j$, in the BS and high-spin (HS) configurations. Here, HS corresponds to equally oriented spins. Since N is the number of centers, there are $N(N-1)/2$ different Js (assuming weak coupling).

In order to perform ab initio calculations of J, it is convenient to define different spin configurations that differ only in the orientation of the spin of one center with respect to the HS configuration. In this case, if the spin of center k of configuration SCk is flipped with respect to the HS configuration, the energy difference is

$$\begin{aligned} E_{\mathrm{HS}} - E_{\mathrm{SCk}} &= \sum_{j\neq k}^{N} E_{\mathrm{HS}}^{(jk)} - E_{\mathrm{BS}}^{(jk)} \\ &= -\sum_{j\neq k}^{N} J_{jk}(2S_jS_k + \min(S_j, S_k)), \end{aligned} \tag{3}$$

where $k = 1, \ldots, N$.

Considering that there are $N+1$ relevant spin configurations (one with the highest spin, and N with the spin flipped in only one center), the coupling constants can be readily obtained, since the number of equations is equal or greater than the number of unknown Js.

3. Results and discussion

Results are presented in two sections. First, Section 3.1 reports the structural and electronic analysis of synthetic mixed-valent multinuclear oxomanganese complexes at the DFT/B3LYP level of theory, including complex **1**: $[Mn^{III}Mn^{IV}(\mu\text{-}O)_2(H_2O)_2(terpy)_2]^{3+}$, complex **2**: $[Mn^{III}Mn^{IV}(O)_2(phen)_4]^{3+}$, complex **3**: $[Mn_3O_4(bpy)_4(H_2O)_2]^{4+}$ and complex **4**: $[Mn_4O_4L_6]^{+}$ ($L = H_2PO_2^-$). The analysis of electronic structure includes computations of exchange coupling constants and comparisons to magnetic measurements. After exploring the capabilities and limitations of the DFT/B3LYP methodology, as applied to benchmark model complexes, Section 3.3 analyzes the electronic and structural properties of biomimetic models of the OEC of PSII.

3.1. Benchmark oxomanganese complexes

3.1.1. Structural characterization

Fig. 1(a) shows the structure of complex **1**, $[Mn^{III}Mn^{IV}(\mu\text{-}O)_2(H_2O)_2(terpy)_2]^{3+}$, in the minimum energy configuration obtained at the DFT/B3LYP level of theory, and the simplified model complex obtained by simplifying the terpyridine ligands (b). The analysis of Mulliken spin-populations indicates anti-ferromagnetic coupling between Mn(1) and Mn(2), with spin-populations of 3.83 and −2.57 a.u., respectively. This description corresponds to

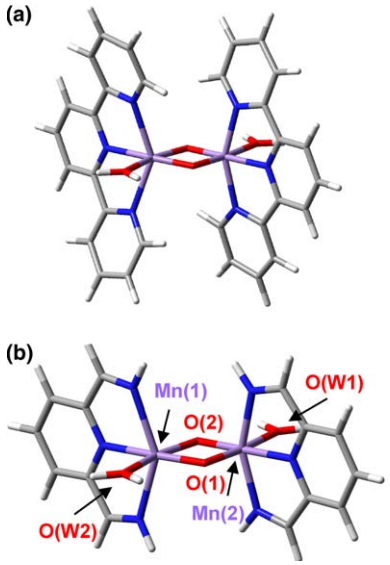

Fig. 1. Molecular structure of complex **1**, $[Mn^{IV}Mn^{III}(\mu\text{-}O)_2(H_2O)_2(terpy)_2]^{3+}$ (terpy = 2,2′:6,2″-terpyridine) (a) and simplified model system (b), optimized at the broken symmetry unrestricted B3LYP level with the following basis set: LACVP for manganese, 6-31G(d) for oxo-bridge oxygens, 6-31G for water oxygens and nitrogen, and 3-21G for carbon and hydrogen. Color key: red = oxygen, blue = nitrogen, gray = carbon, white = hydrogen, and purple = manganese.

Mn(1) with $S = 4/2$ and Mn(2) with $S = -3/2$, in agreement with EPR data [2,99]. Such a spin-electronic state is also consistent with the observed Mn–Mn distances, although the intrinsic disorder of the Mn(III) and Mn(IV) ions in the crystal structure allows one to analyze only metal–ligand distances averaged between both Mn ions.

Table 1 shows the analysis of internal coordinates in the complete model structure of complex **1** (third column) as compared to experimental X-ray diffraction data (second column). It is shown that the calculated and experimental Mn–Mn distance are in excellent agreement with each other, differing only by about 0.001 Å from each other. These findings suggest that larger differences observed in earlier studies [16] are not due to the intrinsic limitations of the DFT/B3LYP methodology but rather due to the limited basis set used, or the structural discrepancy between the simplified model system investigated and the real complex.

Table 1
Comparison between DFT/B3LYP and experimental X-ray inter-atomic distances (Å) in complex **1**

Bond	Experimental[a] (Å)	**1**[b] (Å)	$\mathbf{1}_{sim}$[c] (Å)
Mn–Mn	2.72	2.72	2.71
Mn–O(1,2)	1.81, 1.81	1.81	1.80
Mn–O_w(1,2)	2.01	2.19	2.08
Mn–N(eq)	2.04	2.03	2.06
Mn–N(ax)	2.10, 2.10	2.12	2.18

[a] Metal-averaged X-ray data obtained from disordered crystal [2].
[b] Average values are included for comparison with the metal-averaged X-ray data (**1**). The basis set is LACVP for manganese, 6-31G(d) for oxo-bridge oxygens, 6-31G for water oxygen and nitrogen, 3-21G for carbon and hydrogen.
[c] Simplified model (see text for details) with the same basis set and average values as in footnote b.

In order to investigate the limitations introduced by simplified model systems, where bulky substituents are modeled by smaller ligands, Table 1 (fourth column) reports internal coordinates in the relaxed configuration of the simplified model system shown in Fig. 1 (lower structure). Table 1 shows that, contrary to the complete model structure where the geometry of μ-oxo bridges is in quantitative agreement with experimental data, the simplified model system includes Mn–Mn and Mn–O distances that differ from the experimental value by up to 0.015 Å. Mulliken spin-populations, however, remain almost unchanged (i.e., change only by about 0.05 a.u.).

Complex **2**, $[Mn^{III}Mn^{IV}(\mu\text{-}O)_2(phen)_4]^{3+}$, shown in Fig. 2(a), and a simplified model system, shown in Fig. 2(b), were analyzed in order to investigate the capabilities of the DFT/B3LYP methodology as applied to the description of asymmetric structural features associated with Mn ions of distinct oxidation states (i.e., Mn^{III} and Mn^{IV}). Crystals of this complex are not disordered, so each Mn ion is separately identifiable in the structure. These complexes are mixed-valent oxomanganese dimers with Jahn–Teller distortion associated with the d^4 (Mn^{III}) ion and a non-distorted octahedral d^3 (Mn^{IV}) ion. The geometry around $Mn^{III}(1)$ is typical of an axially elongated d^4 ion with Mn–N(ax) distances ~0.1 Å longer than the equatorial Mn–N(eq) distances.

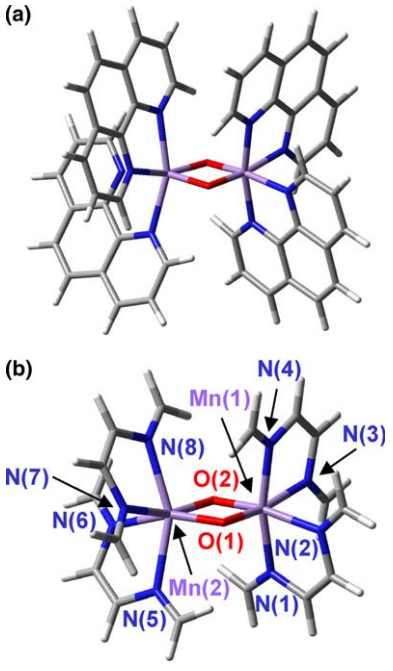

Fig. 2. Molecular structure of complex **2**, $[Mn^{III}Mn^{IV}(O)_2(phen)_4]^{3+}$ (phen = 1,10-phenanthroline) (a) and simplified model system (b), optimized at the broken symmetry unrestricted B3LYP level with the following basis set: LACVP for manganese, 6-31G(d) for oxo-bridge oxygens, 6-31G for water oxygens and N, and 3-21G for carbon and hydrogen. Color key: red = oxygen, blue = nitrogen, gray = carbon, white = hydrogen, and purple = manganese.

Tables 2 and 3 present a detailed comparison between the complete model structure, obtained at the DFT/B3LYP level (column 3), and the X-ray structure (column 2) of complex **2**. Tables 2 and 3 show that there is remarkable agreement of the internal coordinates in complex **2** predicted by the DFT/B3LYP (third column) and the experimental data (second column). In particular, the calculated Mn–Mn distance is in excellent agreement with the X-ray data, differing only by about 0.005 Å. The analysis of spin density on the Mn-ions indicates that there is anti-ferromagnetic coupling between Mn(1) and Mn(2). Formal oxidation numbers III and IV are indicated by the Mulliken spin-populations 3.85 and −2.58 a.u., respectively, in agreement with EPR experiments [4].

As in the case of complex **1**, Tables 2 and 3 (fourth column) indicate that a simplified model complex (with small ligands that simplify large conjugated substituents) provides a less accurate description of the Mn dimer, with an error in the Mn–Mn distance of about 0.03 Å. Spin populations, however, are very similar to those in the original complex (Mn(1) = 3.88 a.u.; Mn(2) = −2.60 a.u.). It is therefore concluded that mixed-valent oxomanganese cluster dimers can be adequately described by simplified model systems according to the DFT/B3LYP methodology so long as the μ-oxo bridges were modeled by sufficiently flexible basis sets. In addition, DFT/B3LYP calculations with complete model structures provide results in quantitative agreement with experiments.

In order to explore the capabilities of the DFT/B3LYP methodology for predicting the structural and electronic properties of higher nuclearity oxomanganese complexes for which low-spin ground electronic states have been reported, complex **3** $[Mn_3O_4(bpy)_4(OH_2)_2]^{4+}$ (Fig. 3(a)) and a simplified model system (Fig. 3(b)) were investigated. Complex **3** was expected to be significantly more challenging than the previously discussed Mn-complexes, since it involves a $(\mu\text{-}O)_2Mn_2$ unit bridged to a third Mn^{4+} ion by an additional O–Mn–O linkage. Since the complex involves an odd number of Mn ions, there is unavoidable spin frustration because only two of the three Mn–Mn pairs can be anti-ferromagnetically coupled. In fact, it has been determined by EPR spectroscopy [5] that the $(\mu\text{-}O)_2Mn_2$ unit has total spin $S = 1$ with either, or both, Mn^{4+} ions in a low spin state $S = 1/2$. In addition, the total spin of the complex in the ground state is $S = 1/2$, indicat-

Table 2
Comparison between DFT/B3LYP and experimental X-ray inter-atomic distances (Å) in complex **2**

Bond	Experimental[a] (Å)	**2**[b] (Å)	$\mathbf{2}_{sim}$[c] (Å)
Mn(1)–Mn(2)	2.71	2.71	2.73
Mn(2)–O(1)	1.84	1.86	1.87
Mn(2)–O(2)	1.86	1.86	1.87
Mn(1)–O(1)	1.77	1.75	1.75
Mn(1)–O(2)	1.78	1.75	1.75
Mn(2)–N(7)	2.12	2.15	2.17
Mn(2)–N(6)	2.12	2.15	2.17
Mn(1)–N(3)	2.10	2.11	2.13
Mn(1)–N(2)	2.09	2.11	2.13
Mn(2)–N(8)	2.22	2.26	2.29
Mn(2)–N(5)	2.24	2.25	2.29
Mn(1)–N(4)	2.03	2.02	2.03
Mn(1)–N(1)	2.04	2.02	2.03

[a] Ref. [4].
[b] LACVP for manganese, 6-31G(d) for oxygen, 6-31G for nitrogen, and 3-21G for carbon and hydrogen.
[c] Simplified model (see Fig. 2(b)), same basis set as in footnote b.

Table 3
Comparison between DFT/B3LYP and experimental X-ray angles (°) in complex **2**

Angle	Experimental[a] (°)	**2**[b] (°)	$\mathbf{2}_{sim}$[c] (°)
Mn(1)–O(1)–Mn(2)	97	97	98
Mn(1)–O(2)–Mn(2)	96	97	98
O(1)–Mn(1)–O(2)	81	80	85
O(1)–Mn(2)–O(2)	85	86	79
N(1)–Mn(1)–O(1)	106	90	91
N(2)–Mn(1)–O(1)	165	164	171
N(3)–Mn(1)–O(1)	96	95	94
N(4)–Mn(1)–O(1)	106	108	98
N(5)–Mn(2)–O(2)	90	91	90
N(6)–Mn(2)–O(2)	170	171	162
N(7)–Mn(2)–O(2)	94	93	97
N(8)–Mn(2)–O(2)	97	99	110

[a] Ref. [4].
[b] LACVP for manganese, 6-31G(d) for oxygen, 6-31G for nitrogen, and 3-21G for carbon and hydrogen.
[c] Simplified model (see Fig. 2(b)), same basis set as in footnote b.

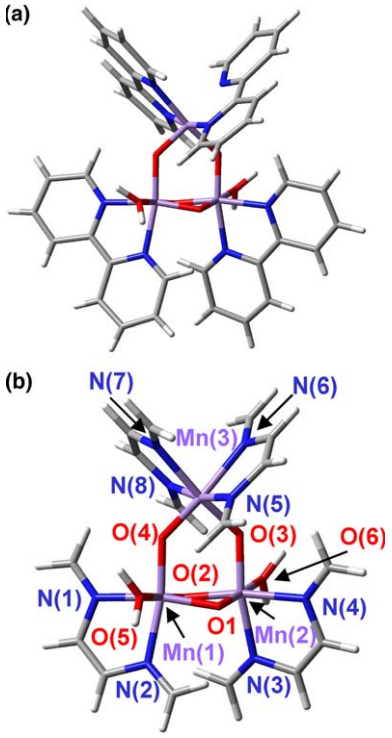

Fig. 3. Molecular structure of complex **3**, $[Mn_3O_4(bpy)_4(OH_2)_2]^{4+}$ (bpy = 2,2′-bipyridine) (a) and simplified model system optimized at the broken symmetry unrestricted B3LYP level (b) with the following basis set: LACVP for manganese, 6-31G(d) for O, 6-31G for nitrogen, and 3-21G for carbon and hydrogen. Color key: red = oxygen, blue = nitrogen, gray = carbon, white = hydrogen, and purple = manganese.

ing that the third Mn^{4+} ion must be in a high-spin state ($S = 3/2$) and anti-ferromagnetically coupled to the $(\mu\text{-}O)_2Mn_2$ unit. The HS state of the complex, with total spin $S = 3/2$, is therefore an excited electronic state.

Tables 4 and 5 compare experimental X-ray diffraction data (second column) to the corresponding values of internal coordinates obtained at the DFT/B3LYP level of theory for the minimum energy structure of complex **3** in a pre-selected LS state compatible with EPR measurements ($Mn_3 = -1/2, -1/2, +3/2$) (third column). The resulting spin populations after geometry optimization are consistent with magnetic measurements (Mn(1) = 1.16 a.u., Mn(2) = 1.15 a.u., Mn(3) = −2.78 a.u.). Furthermore, the minimum energy geometry of the complex is found to be in excellent agreement with X-ray measurements, predicting a single Mn–Mn distance shorter than 2.7 Å and two Mn–Mn distances larger than 3.2 Å.

Tables 4 and 5 compare the experimental X-ray diffraction data (second column) to the corresponding values in the simplified model system shown in Fig. 3(b), when prepared in the pre-selected LS states ($Mn_3 = -1/2, -1/2, +3/2$) (fourth column) and ($Mn_3 = +1/2, -3/2, +3/2$) (fifth column), as well as in the HS state ($Mn_3 = +3/2, +3/2, -3/2$) (sixth column). It is found that the geometry of the oxomanganese complex is remarkably *insensitive* to the specific spin-state of individual Mn ions in the cluster. All of these models are in excellent agreement with the experimental X-ray diffraction data, suggesting that multiple spin-states could coexist and inter-convert with negligible conformational changes if they were energetically accessible.

However, the analysis of the energetics of various low-lying spin-states of complex **3** indicates that the DFT/B3LYP level of theory erroneously predicts the ground electronic state to be the HS state ($Mn_3 = +3/2, +3/2, -3/2$), in disagreement with EPR measurements [5]. Furthermore, the DFT/B3LYP methodology erroneously predicts that the LS states ($Mn_3 = +1/2, -3/2, +3/2$) and ($Mn_3 = +1/2, +1/2, -3/2$) are, respectively, 21 kcal/mol and 41 kcal/mol above the ground electronic state. This remarkable failure of the DFT/B3LYP methodology adds one more example to the list of high-valent transition metal complexes in which DFT provides an unreliable description of the energetics of the low-lying spin-electronic states [31,35,39,81–83,100].

An unreliable description of the energetics of the low-lying spin-electronic states of mixed-valent oxomanganese complexes is a significant obstacle to the application of DFT to mechanistic studies of the OEC, where until now the performance of DFT has raised little concern [23,80]. However, the problem is not surprising, especially considering that similar shortcomings have already been reported in studies of other high-valent transition metal complexes [31,35,81–83,100], and that the B3LYP hybrid functional has been parameterized according to properties of a reference set of molecules containing only second- and third-period atoms and hydrogen, excluding all transition-metal

Table 4
Comparison between DFT/B3LYP and experimental X-ray inter-atomic distances (Å) in complex **3**

Bond	Experimental[a] (Å)	**2**[b] (Å)	**2**(LS)$_{sim}$[c] (Å)	**2**(LS)$_{sim}$[d] (Å)	**2**(HS)$_{sim}$[e] (Å)
Mn(1)–Mn(2)	2.68	2.6	2.67	2.68	2.68
Mn(1)–Mn(3)	3.25	3.27	3.26	3.24	3.26
Mn(2)–Mn(3)	3.26	3.27	3.26	3.26	3.26
Mn(1)–O(2)	1.79	1.74	1.74	1.76	1.78
Mn(1)–O(4)	1.83	1.831	1.82	1.80	1.82
Mn(1)–N(2)	2.04	2.05	2.07	2.08	2.09
Mn(2)–O(2)	1.81	1.84	1.84	1.82	1.82
Mn(2)–O(3)	1.85	1.81	1.81	1.82	1.82
Mn(2)–N(3)	2.04	2.05	2.07	2.08	2.09
Mn(3)–O(3)	1.76	1.77	1.77	1.76	1.76
Mn(3)–N(8)	1.99	2.02	2.03	2.03	2.03
Mn(3)–N(6)	2.07	2.11	2.13	2.13	2.12
Mn(1)–O(1)	1.80	1.84	1.83	1.82	1.82
Mn(1)–O(5)	2.04	2.08	2.07	2.09	2.09
Mn(1)–N(1)	2.05	2.04	2.07	2.08	2.09
Mn(2)–O(1)	1.82	1.74	1.74	1.77	1.78
Mn(2)–O(6)	2.05	2.08	2.08	2.09	2.09
Mn(2)–N(4)	2.06	2.04	2.07	2.09	2.09
Mn(3)–O(4)	1.77	1.77	1.76	1.76	1.76
Mn(3)–N(5)	2.01	2.02	2.04	2.03	2.03
Mn(3)–N(7)	2.09	2.02	2.13	2.13	2.12

[a] Ref. [5].
[b] LACVP for manganese, 6-31G(d) for oxygen, 6-31G for nitrogen, and 3-21G for carbon and hydrogen, and formal spin state $Mn_3 = (-1/2, -1/2, +3/2)$.
[c] Simplified model (see Fig. 3(b)), same basis set and spin state as in footnote b.
[d] Same as footnote c but with formal spin states $Mn_3 = (+1/2, -3/2, +3/2)$.
[e] Same as footnote c but with formal spin states $Mn_3 = (+3/2, +3/2, -3/2)$.

Table 5
Comparison between DFT/B3LYP and experimental X-ray angles (°) in complex **3**

Angle	Experimental[a] (°)	**2**[b] (°)	**2**(LS)$_{sim}$[c] (°)	**2**(LS)$_{sim}$[d] (°)	**2**(HS)$_{sim}$[e] (°)
O(2)–Mn(1)–O(1)	84	82	82	82	82
O(2)–Mn(1)–O(4)	98	99	98	98	96
O(2)–Mn(1)–O(5)	176	176	176	175	176
O(1)–Mn(1)–O(5)	96	93	94	93	93
O(1)–Mn(1)–O(4)	96	94	96	97	96
O(2)–Mn(2)–O(3)	95	95	94	97	96
O(2)–Mn(2)–O(6)	97	93	94	94	93
O(3)–Mn(3)–O(4)	101	97	98	98	98
O(4)–Mn(1)–O(5)	86	81	83	84	84
O(2)–Mn(2)–O(1)	82	82	82	81	82
O(1)–Mn(2)–O(3)	97	99	99	96	96
O(1)–Mn(2)–O(6)	177	175	175	175	176
O(3)–Mn(3)–O(6)	86	81	83	84	84

[a] Ref. [5].
[b] LACVP for manganese, 6-31G(d) for oxygen, 6-31G for nitrogen, and 3-21G for carbon and hydrogen, and formal spin state $Mn_3 = (-1/2, -1/2, +3/2)$.
[c] Simplified model (see Fig. 3(b)), same basis set and spin state as in footnote b.
[d] Same as footnote c but with formal spin states $Mn_3 = (+1/2, -3/2, +3/2)$.
[e] Same as footnote c but with formal spin states $Mn_3 = (+3/2, +3/2, -3/2)$.

elements. Considering that the B3LYP functional has been identified as the most successful DFT method in an overwhelming number of systematic investigations in many areas of chemical research, these findings are expected to stimulate the development of more reliable functionals. In fact, some improvement in the description of energy splittings between low-lying spin-electronic states of transition metal complexes has already been achieved by re-parameterization of the B3LYP hybrid functional through adjustment of the amount of exact exchange admixture [31,39]. Such a re-parameterization of the B3LYP functional [31], however, only partially corrects the energy splitting between LS and HS states of complex **3** (a correction smaller than 4 kcal/mol), failing to provide the correct relative stability of LS and HS states.

Other possible corrections have been considered, including the perturbational effect of counter ions, the effect of possible distortions induced by the crystal and the effect of exchange coupling. It was found that the inclusion in the model of crystallographic counter ions (e.g., ClO_4^-), placed at the X-ray positions relative to the oxomanganese complex, reduces only slightly (i.e., by less than 1.5 kcal/mol) the difference in energy between the HS(+3/2, +3/2, −3/2) and LS(−1/2, −1/2, +3/2) states. These calculations thus show that the perturbational effect of counter ions does not alter the order of HS and LS energy levels. In addition, packing effects are not expected to be important since the configuration of the complex obtained by geometry optimization at the DFT/B3LYP level is found to be in excellent agreement with the X-ray model structure.

Finally, the capabilities of the DFT/B3LYP methodology are investigated as applied to the description of the mixed-valent oxomanganese complex **4** $[Mn_4O_4L_6]^+$, with $L = Ph_2PO_2^-$, shown in Fig. 4(a), which is modeled according to the reduced structure $[Mn_4O_4L'_6]^+$, with $L' = H_2PO_2^-$, shown in Fig. 4(b). This oxomanganese tetramer is paramagnetic in the ground electronic state and exhibits intense EPR spectra in solution, indicating an odd-spin ground state ($S \geqslant 3/2$). The specific spin states of the individual Mn ions in the complex, however, have not been characterized experimentally. It has only been suggested that the geometry of the cluster is consistent with the assignment of oxidation numbers (III, IV, IV, IV), although no Jahn–Teller elongation has been observed for any of the Mn-ions in the crystal [89]. Tables 6 and 7 show the comparison between the architecture of the complex obtained from X-ray diffraction data and that predicted by the DFT/B3LYP level of theory when preselecting the high-spin state (−4/2, +3/2, +3/2, +3/2), with total spin $S = 5/2$, consistent with magnetic measurements. DFT/B3LYP geometry optimizations were performed imposing C_s symmetry, since higher symmetry conditions would not be consistent with the desired constraints of total spin, total charge, individual atomic spins and oxidation states. The resulting Mulliken spin populations, after geometry optimization, are $Mn_4 =$ (−3.78, +2.88, +2.88, +2.92), showing negligible spin contamination and formal total spin $S = 5/2$, consistent with magnetic measurements. The resulting structure of the oxomanganese cubane cluster involves significant trigonal distortion from tetrahedral symmetry, creating a trigonal pyramidal Mn_4 core with shorter base Mn–O distances (e.g., Mn(2)–O and Mn(4)–O) and longer Mn(apical)–Mn(base) bond lengths (e.g., Mn(1)–Mn(2) and Mn(1)–Mn(4)). The average Mn(apical)–Mn(base) and Mn(base)–Mn(base) distances in (**4**) are 2.95 and 2.86 Å, in very good agreement with the experimental values 2.93

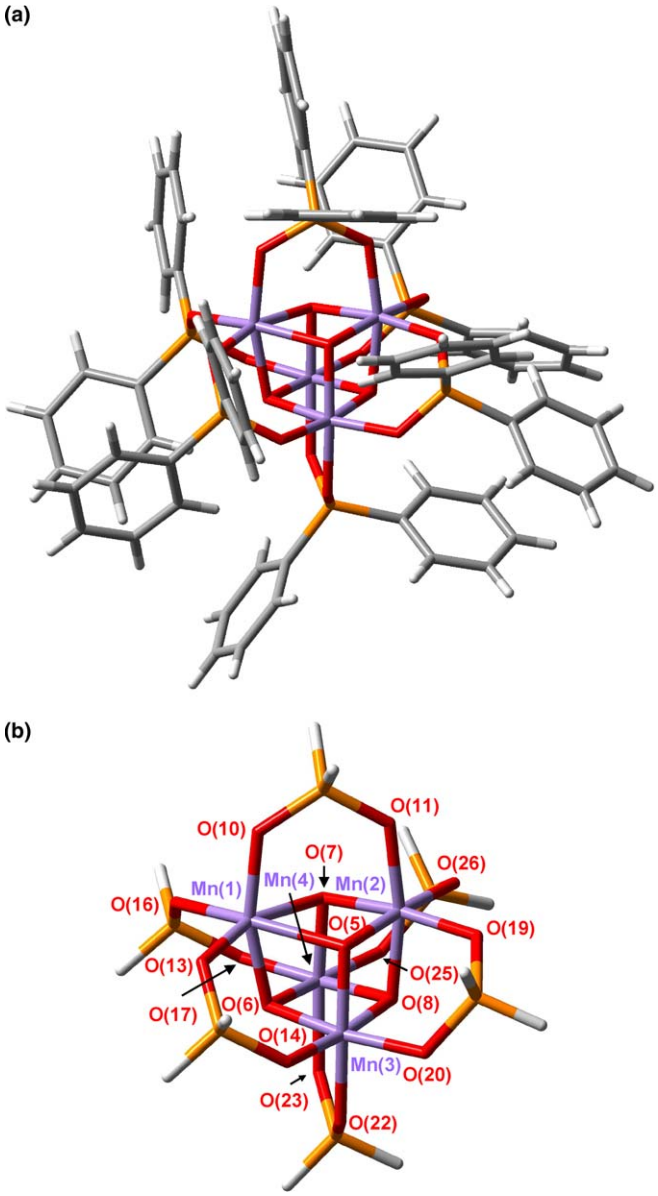

Fig. 4. Molecular structure of complex **4**, $[Mn_4O_4L_6]^+$ ($L = Ph_2PO_2^-$) (a) and simplified model system (b), optimized at the broken symmetry unrestricted B3LYP level with the following basis set: LACVP for manganese, 6-31G(2df) for oxo-bridge oxygens, 6-31G for oxygen, 3-21G* for phosphorous, and 3-21G for carbon and hydrogen. Color key: red = oxygen, gray = carbon, white = hydrogen, and purple = manganese, orange = phosphorous.

Table 6
Comparison between DFT/B3LYP and experimental X-ray inter-atomic distances (Å) in complex **4**

Bond	Experimental[a] (Å)	**2**[b] (Å)
Mn(1)–Mn(3)	2.91	2.93
Mn(1)–Mn(2)	2.98	3.01
Mn(1)–Mn(4)	2.90	2.93
Mn(2)–Mn(3)	2.84	2.80
Mn(2)–Mn(4)	2.83	2.80
Mn(3)–Mn(4)	2.86	2.84
Mn(1)–O(5)	2.05	2.13
Mn(1)–O(6)	1.92	1.90
Mn(1)–O(7)	2.04	2.13
Mn(2)–O(5)	1.89	1.85
Mn(2)–O(7)	1.90	1.85
Mn(2)–O(8)	1.91	1.88
Mn(3)–O(5)	1.87	1.83
Mn(3)–O(6)	1.91	1.90
Mn(3)–O(8)	1.90	1.88
Mn(4)–O(6)	1.91	1.90
Mn(4)–O(7)	1.85	1.83
Mn(4)–O(8)	1.89	1.88
Mn(1)–O(10)	1.90	1.90
Mn(1)–O(13)	1.94	1.98
Mn(1)–O(16)	1.97	1.98
Mn(2)–O(11)	1.89	1.90
Mn(2)–O(19)	1.91	1.91
Mn(2)–O(26)	1.92	1.91
Mn(3)–O(14)	1.89	1.88
Mn(3)–O(22)	1.91	1.92
Mn(3)–O(20)	1.90	1.91
Mn(4)–O(17)	1.88	1.88
Mn(4)–O(23)	1.93	1.92
Mn(4)–O(25)	1.91	1.91

[a] Ref. [89].
[b] Simplified model (Fig. 4(b)) with LACVP for manganese, 6-31G(2df) for oxo-bridge oxygens, 6-31G for oxygen, 3-21G* for phosphorous, and 3-21G for carbon and hydrogen.

Table 7
Comparison between DFT/B3LYP and experimental X-ray angles (°) in complex **4**

Angle	Experimental[a] (°)	**2**[b] (°)
O(5)–Mn(1)–O(7)	78	74
O(5)–Mn(1)–O(6)	79	77
O(6)–Mn(1)–O(7)	79	77
O(5)–Mn(2)–O(7)	85	88
O(5)–Mn(2)–O(8)	82	82
O(7)–Mn(2)–O(8)	82	82
O(5)–Mn(3)–O(6)	84	85
O(5)–Mn(3)–O(8)	83	82
O(6)–Mn(3)–O(8)	82	82
O(6)–Mn(4)–O(7)	84	84
O(6)–Mn(4)–O(8)	82	81
O(7)–Mn(4)–O(8)	84	82

[a] Ref. [89].
[b] Simplified model (Fig. 4) with LACVP for manganese, 6-31G(2df) for oxo-bridge oxygens, 6-31G for oxygen, 3-21G* for phosphorous, and 3-21G for carbon and hydrogen.

and 2.84 Å, respectively. Note that the Mn–Mn distances are 0.1–0.2 Å longer than the typical 2.7 Å Mn–Mn distances in oxomanganese dimers $[Mn_2O_2]^{3+/4+}$ cores [7].

Table 8
Oxidation numbers, Mulliken spin population analyses (in parenthesis) and ab initio exchange coupling constants, J_{ij}, computed at the DFT B3LYP level with the TZV basis set for the high-valent multinuclear oxomanganese complexes **1**, **2** and **3** introduced in the text

Complex	Mn(1)	Mn(2)	Mn(3)	J_{12} (cm^{-1})	J_{23} (cm^{-1})
1	III (+3.8)	IV (−2.6)	–	298 (300)*	–
2	III (+3.9)	IV (−2.6)	–	295 (268–300)*	–
3	IV (−1.2)	IV (−1.2)	IV(+2.8)	211 (182)*	70 (98)*

The symbol * indicates experimental values of coupling constants [5,101–103].

3.1.2. Magnetic properties

Table 8 compares exchange coupling constants for synthetic oxomanganese complexes **1**–**3** to readily available experimental data [5,101–103]. Exchange coupling constants are obtained at the DFT/B3LYP level according to the methodology outlined in Section 2.2 and show very good agreement with experimental data. These results serve to validate the DFT/B3LYP level as applied to the description of magnetic properties of oxomanganese complexes in pre-defined spin-electronic states. The following discussion analyzes the origin of magnetic exchange couplings in oxomanganese complexes on the basis of electronic delocalization.

In the weak-coupling (localized) limit, atomic d-orbitals remain singly occupied and the spin states are essentially localized on individual metal centers. Therefore, the ground state of a multinuclear complex with weak internuclear interactions involves antiparallel coupling between spin states localized on different centers. Metal–metal interactions, however, tend to induce electronic delocalization over multiple centers, forming bonding- and antibonding-orbitals by either direct overlap of atomic orbitals, or superexchange.

The exchange coupling constants are determined by the splitting between energy-levels as defined by Eq. (2) (Section 2.2). In the weak-coupling limit, spin polarization is responsible for the separation between occupied and vacant orbitals, whereas in the delocalized limit, splitting between bonding and antibonding molecular orbitals is caused by metal–metal interactions. The strength of the interactions thus determines the extent of electron delocalization and consequently the resulting geometry and the magnetic properties of the complex.

In the broken-symmetry state, α and β electronic densities are allowed to localize on different atomic centers. These relaxed symmetry requirements allow for substantial interactions mediated by d-orbitals of Mn and p-orbitals of the ligands. The extent to which molecular orbitals involved in broken-symmetry states are delocalized over the metal centers can be determined by the analysis of atomic orbital composition.

Tables 9–11 show the decomposition of molecular orbitals with significant Mn d-orbital contributions, in terms of the squared amplitudes of the expansion coefficient associated with the atomic orbitals of manganese, bridging oxygens, and the rest of the ligands. For convenience, atomic

Table 9
Decomposition of molecular orbitals of complex **1**, with significant contributions of Mn atomic d-orbitals, into atomic orbital contributions from Mn and bridging ligands

MO[a]	Mn(1)[b]	Mn(2)[b]	O(3)	O(4)	Ligand[c]
102α	$0.42d_{z^2}$	0.04	0.04	0.01	0.40
100α	$0.15d_{xz}$, d_{yz}	$0.06d_{xz}$, d_{yz}	0.00	0.22	0.15
99α	$0.19d_{xz}$, d_{yz}	$0.12d_{xz}$, d_{yz}	0.30	0.02	0.10
97α	$0.09d_{xy}$	0.04	0.25	0.13	0.21
100β	0.03	$0.22d_{xz}$, d_{yz}	0.29	0.00	0.18
99β	0.03	$0.23d_{xz}$, d_{yz}	0.03	0.43	0.06
97β	0.02	$0.11d_{x^2-y^2}$	0.05	0.11	0.19
96β	0.03	$0.21d_{x^2-y^2}$	0.03	0.16	0.16

[a] α and β HOMOS are 102α and 101β, respectively.
[b] Atomic orbital contributions to molecular orbitals are listed in order of decreasing weight.
[c] The rest of manganese ligands taken together.

Table 10
Decomposition of molecular orbitals of complex **2**, with significant contributions of Mn atomic d-orbitals, into atomic orbital contributions from Mn and bridging ligands

MO[a]	Mn(1)[b]	Mn(2)[b]	O(3)	O(4)	Ligand[c]
110α	$0.37d_{z^2}$	0.03	0.02	0.02	0.44
106α	$0.26d_{yz}$	$0.08d_{yz}$	0.12	0.12	0.20
104α	$0.16d_{xz}$	$0.12d_{xz}$	0.20	0.20	0.02
102α	0.19	0.04	0.15	0.15	0.21
105β	0.02	$0.16d_{xz}$	0.22	0.22	0.07
104β	0.03	$0.22d_{yz}$	0.16	0.16	0.22
102β	0.04	$0.32d_{x^2-y^2}$	0.16	0.16	0.14

[a] α and β HOMOS are 110α and 109β, respectively.
[b] Atomic orbital contributions to molecular orbitals are listed in order of decreasing weight.
[c] The rest of manganese ligands taken together.

orbitals are defined in terms of a Cartesian coordinate system for each Mn center where the *z*-axis is perpendicular to the O–Mn–O plane and the *y*-axis is chosen along the Mn–Mn direction (see Fig. 5). In such a coordinate frame, the octahedral t_{2g} orbitals of each Mn center correspond to the atomic orbitals $d_{x^2-y^2}$, d_{yz}, and d_{xz}, while the e_g orbitals correspond to atomic orbitals d_{z^2} and d_{xy}.

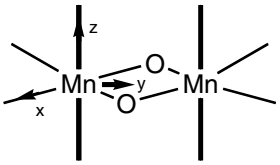

Fig. 5. Cartesian coordinate system associated to each Mn atom.

Direct metal–metal interactions arise from the overlap of atomic d-orbitals on different Mn centers. These direct metal–metal interactions, however, are small in complexes **1**–**3** due to large Mn–Mn separations (i.e., negligible overlaps of atomic orbitals with Mn–Mn distances >2.65 Å) [104]. Therefore, the magnetic coupling is dominated by superexchange via the bridging ligands [104,105]. Because of the low symmetry, there is a large number of possible superexchange pathways (depicted in Fig. 6), although only a few of them make significant contributions to the overall magnetic exchange.

For complexes **1** and **2**, only pathways that involve d_{xz} and d_{yz} orbitals in both Mn centers, denoted $J_{xz/xz}$ and $J_{yz/yz}$, respectively, form efficient symmetric superexchange pathways due to the significant overlap between orbitals d_{xz} and d_{yz} and the relevant out-of-plane pπ orbitals associated with oxo-bridging ligands. In contrast, the symmetric exchange pathway $J_{x^2-y^2/x^2-y^2}$ has a much smaller contribution since the in-plane p_π orbitals of the oxo-ligands overlap with only one Mn center, being nearly orthogonal to the d orbitals of the other Mn center. These arguments are supported by the composition of molecular orbitals presented in Tables 9 and 10, where it is shown that the molecular orbitals with significant contributions from atomic orbitals $d_{x^2-y^2}$ are essentially localized on one Mn center. Further, large contributions from the bridging O^{2-} indicate that the superexchange mechanism

Table 11
Decomposition of molecular orbitals of complex **3**, with significant contributions of Mn atomic d-orbitals, into atomic orbital contributions from Mn and bridging ligands

MO[a]	Mn(1)[b]	Mn(2)[b]	Mn(3)[b]	O(4)	O(5)	O(6)	O(7)	Ligand[c]
125α	$0.13d_{xz}$	$0.11d_{xz}$	0.19[d]	0.01	0.01	0.14	0.16	0.01
128α	0.03	0.04	0.24[d]	0.01	0.01	0.18	0.19	0.09
129α	0.02	0.02	0.12	0.04	0.04	0.19	0.19	0.07
130α	$0.16d_{xz}$, d_{yz}	$0.19d_{xz}$, d_{yz}	0.03	0.07	0.06	0.06	0.06	0.05
135α	$0.20d_{xz}$, d_{yz}	$0.14d_{xz}$, d_{yz}	0.04	0.06	0.10	0.09	0.07	0.08
123β	$0.23d_{xy}$, $d_{x^2-y^2}$	$0.28d_{xy}$, $d_{x^2-y^2}$	0.01	0.08	0.10	0.02	0.02	0.06
124β	$0.16d_{xy}$, $d_{x^2-y^2}$	$0.09d_{xy}$, $d_{x^2-y^2}$	0.05	0.07	0.04	0.11	0.10	0.05
125β	$0.18d_{xz}$, d_{yz}	$0.11d_{xz}$, d_{yz}	0.03	0.02	0.06	0.07	0.09	0.12
126β	0.06	0.19	0.01	0.19	0.07	0.03	0.10	0.14
127β	0.18	0.12	0.02	0.09	0.16	0.09	0.00	0.10
128β	0.03	$0.07d_{xz}$, d_{yz}	0.08	0.07	0.06	0.09	0.20	0.10
129β	$0.15d_{xz}$	$0.09d_{xz}$	0.10	0.03	0.07	0.16	0.09	0.04

[a] α and β HOMOS are 135α and 134β, respectively.
[b] Atomic orbital contributions to molecular orbitals are listed in order of decreasing weight.
[c] The rest of manganese ligands taken together.
[d] The atomic orbital has d_{z^2} shape, with its longer direction parallel to the Mn(1)–Mn(2)–Mn(3) plane.

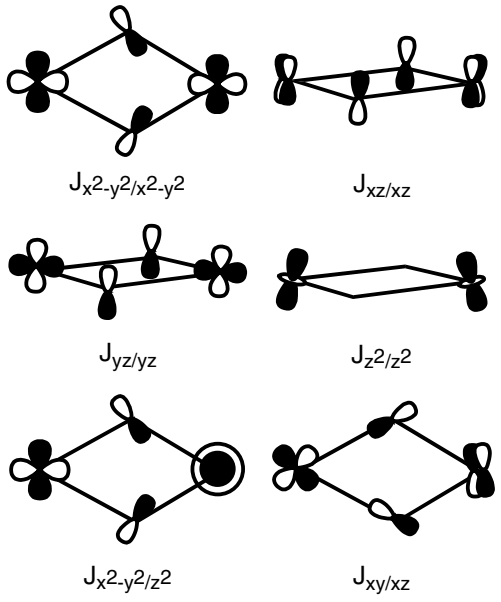

Fig. 6. Representation of exchange pathways corresponding to the [Mn(1)Mn(2)(μ-O)$_2$] moiety of complexes **1**–**3**. Symmetric pathways: $J_{x^2-y^2/x^2-y^2}$, $J_{xz/xz}$, and $J_{yz/yz}$ and J_{z^2/z^2}, cross pathways: $J_{x^2-y^2/z^2}$, and $J_{xy/xz}$.

mediated by the bridging O^{2-} make significant contributions to the overall magnetic exchange.

Tables 9 and 10 show that α-orbitals are more delocalized and therefore more involved in the exchange pathways, probably because of the deficiency of electronic charge on the β-Mn^{IV}(2) center. The greatest delocalization corresponds to the 99α orbital which is therefore the principal exchange pathway.

Complexes **1** and **2** have very similar exchange coupling constants due to the underlying similarities of their corresponding electronic structures. The contribution from Mn and O^{2-} ligands are slightly smaller in **1** than in **2**, with a concomitantly greater contribution from other ligands, showing that the latter are better donors.

In the case of complex **3**, the presence of an extra oxo-bridge creates a different bond framework giving rise to a particular pattern of delocalization pathways. Most notorious is the presence of a pathway including three manganese centers with d_{xz} orbitals of Mn(1) and Mn(2), and d_{z^2} type orbitals of Mn(3), overlapping with out-of-plane p-orbitals on the O^{2-} that forms the additional oxo-bridge. The underlying structure becomes evident from the analysis, presented in Table 11, of molecular orbital 125α.

Other superexchange pathways, involving d_{xz} orbitals of Mn(1) and Mn(2) involve smaller contributions of the bridging oxygens (130α,135α, and 125β, Table 11) when compared to the dimanganese complexes, since these orbitals are involved in molecular orbitals that comprise centers of the additional ring. This effect reduces the efficiency of the symmetric $J_{x^2-y^2/x^2-y^2}$ pathway. Table 11 also shows some other orbitals with important contributions of Mn(1) and Mn(2) (e.g., 123β and 124β). However, these orbitals do not contribute significantly to the exchange coupling since the corresponding atomic orbitals do not form allowed pathways (see Fig. 6).

In summary, the analysis of the electronic structure of di- and tri-nuclear Mn-complexes show that the most important exchange interactions between Mn(1) and Mn(2) centers involve symmetric super-exchange pathways $J_{xz/xz}$ and $J_{yz/yz}$ mediated by the overlap of orbitals d_{xz} and d_{yz} of Mn with the out-of-plane p_π orbitals of the μ-oxo bridges. Although the number of pathways and contributions from Mn(1) and Mn(2) are similar in the three complexes, J_{12} is smaller in **3** than in the other two complexes, partly due to the smaller contributions of intermediate bridging O^{2-}. The analysis of the electronic structure of the Mn trimers shows that the most important exchange interactions between Mn centers in the additional O–Mn–O linkage involve d_{xz} orbitals on Mn(1) and Mn(2), and a d_z^2 type orbital in Mn(3) overlapping with out-of-plane p orbitals of the bridging O^{2-}. Mn(3) is weakly coupled to the other metal centers, since there is only one pathway (involving orbital 125α), which contributes to make J_{13} the smallest exchange coupling constant. The corresponding pathways make antiferromagnetic contributions to the overall exchange coupling constant, simply because all of the involved atomic orbitals of each Mn center are occupied.

3.2. Spin-density profiles

In order to analyze the spin density profiles, Tables 12 and 13 present the Mulliken spin population analysis of complexes **1** and **3**, respectively. It is shown that the manganese spin densities change, in these oxo-manganese compounds, by less than 0.3 a.u. Therefore, the formal oxidation state is always consistent with the Mulliken spin population. Further, no appreciable spin delocalization is observed in high or low spin-states. These results can be contrasted to the analogous iron complexes (see Ref. [85], and references cited therein) that show more delocalized spin density profiles, with Mulliken populations almost one full unit below their formal values. Further, these iron-analogue complexes typically show that the low spin states are significantly more delocalized.

Table 12
Mulliken spin densities of the metal centers and ligating atoms in complex **1**

Atom	Spin population
Mn(1)	+3.83
Mn(2)	−2.57
O(3)	−0.24
O(4)	−0.18
O(5)	+0.01
O(6)	+0.00
N(7)	+0.05
N(8)	−0.03
N(9)	+0.05
N(10)	+0.02
N(11)	+0.03
N(12)	+0.02

Table 13
Mulliken spin densities of the metal centers and ligating atoms in complex **3**

Atom center	Spin density
Mn(1)	+1.16
Mn(2)	+1.15
Mn(3)	−2.78
O(4)	−0.18
O(5)	−0.22
O(6)	−0.14
O(7)	−0.11
O(8)	+0.01
O(11)	+0.01
N(14)	−0.01
N(15)	−0.04
N(26)	−0.01
N(27)	−0.04
N(38)	+0.03
N(39)	+0.04
N(50)	+0.03
N(51)	+0.05

For example, the iron complex $[(6\text{-me}_3\text{-tpa})Fe^{III}(\mu\text{-}O)_2Fe^{IV}(6\text{-me}_3\text{-tpa})]^{3+}$ [85] which is structurally related to complexes **1** and **2**, has spin densities on Fe^{III} and Fe^{IV} similar to the corresponding densities in Mn^{III} and Mn^{IV}, respectively, in complexes **1** and **2**. However, the iron ions have an additional formal electron relative to manganese. The two extra electrons in the complex, formally in the iron centers, are delocalized along the ligands, including one full spin unit over the O^{2-} bridging ligands, and the other unit delocalized on the rest of the molecule. This trend is probably due to the tendency of the unpaired electrons in transition metals to accommodate in five d-orbitals.

3.3. OEC model complexes

This section analyzes two biomimetic models of the OEC of PSII at the DFT/B3LYP level of theory. These models are the hydrated oxomanganese model complex Mn_3CaO_4Mn (see Fig. 7(a)), chelated only by water, hydroxyl ligands, and chloride, and the same metal cluster ligated by formates and imidazole ligands, mimicking the coordination of amino-acid residues suggested by studies where the surrounding biomolecular environment is explicitly considered [106,107] (see Fig. 7(b)). These model complexes are particularly relevant as biomimetic systems since, in contrast to other Mn cubane structures [89,108,109], they share most of the structural elements with the 3+1 Mn-tetramer of the OEC of PSII. Understanding the electronic and structural properties is thus expected to shed light on the design of new synthetic complexes that might catalyze oxygen evolution by photocatalytic water splitting when associated with suitable sources and sinks of electrons and protons.

Table 14 shows the analysis of internal coordinates associated with the fully relaxed molecular structure of the hydrated Mn_3CaO_4Mn cluster shown in Fig. 7(a) (second column) as compared to the configuration of the OEC of

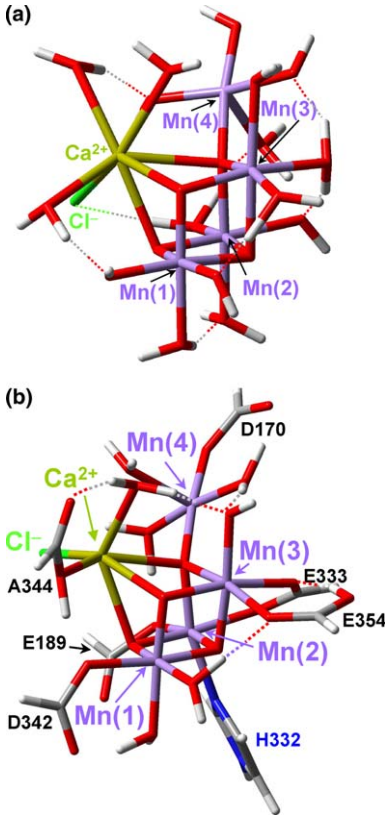

Fig. 7. (a) Hydrated OEC cluster $[Mn_4O_4CaCl(H_2O)_{10}(OH)_6]^+$ ligated by water and hydroxide anions. (b) Model of the OEC cluster chelated by formate, imidazole, water and hydroxide ligands. Optimized structures are obtained at the broken symmetry unrestricted B3LYP level. The basis set comprises LACVP for manganese and calcium, 6-31G(2df) Cl, O(5), O(6), O(7), and O(8); and 3-21G for oxygen and H of water and hydroxide moieties. Color key: red = oxygen, blue = nitrogen, gray = carbon, white = hydrogen, and purple = manganese, green = chlorine, yellow = calcium.

PSII in the 1S5L X-ray model (fifth column). These results show that even in the absence of proteinaceous ligands, the conformation of the hydrated Mn_3CaO_4Mn cluster is remarkably similar to the oxomanganese cluster in PSII. In addition, the predicted ground electronic state is the high-valent configuration of oxidation numbers Mn_4(IV, IV,III,III), consistent with the S_1-state of the OEC of PSII as indicated by EPR and X-ray spectroscopy [10,110–117]. These findings suggest that the protein environment, surrounding the Mn_3CaO_4Mn cluster of PSII, must conform natural selection to the electronic and structural properties intrinsic to the inorganic oxomanganese cluster.

Key structural features of the hydrated Mn_3CaO_4Mn cluster are the hydrogen-bonds linking water molecules coordinated to pairs of metal ions, including Mn(1)–Mn(2), Mn(1)–Mn(3), Mn(2)–Mn(3), and Mn(2)–Mn(4) and Ca^{2+}–Mn(4). It is also found that chloride plays an important structural role in this model system by stabilizing hydrogen-bonded water molecules and Ca^{2+} through complementary electrostatic interactions. These results therefore indicate that the fully hydrated Mn_3CaO_4Mn

Table 14
Inter-atomic distances (Å) in the hydrated Mn_3O_4CaMn and Mn_3O_4SrMn complexes obtained at the UDFT/B3LYP level of theory, compared to the crystallographic model of the OEC of PSII (protein databank accession code 1S5L) [27]

Bond	Mn_3O_4CaMn hydrated[a] (Å)	Mn_3O_4SrMn hydrated[a] (Å)	Mn_3O_4-CaMn with ligand[a] (Å)	Experimental X-ray[b] (Å)
Mn(1)–Mn(2)	2.71	2.71	2.77	2.7
Mn(1)–Mn(3)	2.81	2.81	2.76	2.7
Mn(2)–Mn(3)	2.89	2.88	2.87	2.7
Mn(2)–Mn(4)	3.56	3.56	3.42	3.2
Mn(3)–Mn(4)	3.49	3.48	3.74	3.2
Ca/Sr–O(5)	2.46	2.59	2.57	2.5
Ca/Sr–O(7)	2.60	2.72	2.56	2.5
Ca/Sr–O(8)	2.53	2.70	2.42	2.5
Mn–O[c]	1.89	1.88	1.89	1.8

[a] Basis sets: LACVP for manganese and Ca, 6-31G(2df) for O(5), O(6), O(7), and O(8), 6-31G(d) for Cl, and 3-21G for oxygen and hydrogen atoms of water and hydroxide moieties.

[b] The crystallographic Mn–O and Mn–Mn distances are broadly consistent with EXAFS measurements of the OEC. These indicate a first coordination Mn shell (presumably Mn–O) at 1.8–2.0 Å, as well as three Mn–Mn 2.7 Å distances and one or two Mn–Mn distances around 3.3 Å [128]. The Ca–O distances in the table are derived entirely from the crystallographic model.

[c] Mean value.

cluster is stabilized by inter-ligand interactions in addition to the stabilization due to the coordination of specific ligands. Considering the structural similarity between the OEC of PSII and the hydrated Mn_3CaO_4Mn cluster, even in the absence of proteinaceous ligands, it is natural to expect that a wide range of synthetic oxomanganese complexes, based on the cuboidal '3+1 Mn-tetramer' but with different types of ligands [89,108,109], should be feasible. Even analogous complexes, where Ca^{2+} and Cl^- are substituted by other ionic cofactors (e.g., Sr^{2+} and $CH_3CO_2^-$) are expected to exhibit only small structural differences, as implied by the third column of Table 14, which presents data obtained from a structural model in which Ca^{2+} has been substituted by Sr^{2+}. These results are consistent with X-ray absorption spectroscopy (XAS) data of Sr^{2+}-reconstituted PSII samples showing rather small changes (0.014 Å) in the Mn–Mn distances [118–121]. In agreement with XAS studies, Table 14 (third column) shows that similarly small structural changes are observed in the hydrated model when Ca^{2+} is replaced by Sr^{2+}: the Mn(2)–Mn(3) and Mn(3)–Mn(4) distances decrease by only 0.01 Å. It is, however, noteworthy that the Sr^{2+}–oxygen distance is markedly greater than the Ca^{2+}–oxygen distance due to the larger ionic radius of Sr^{2+}.

The oxomanganese model complex shown in Fig. 7(b) was analyzed at the DFT/B3LYP level of theory, in order to investigate the effect of coordination of specific proteinaceous ligands to the Mn_3CaO_4Mn cluster. Inclusion of the explicit perturbational influence of the biomolecular environment, which surrounds the Mn_3CaO_4Mn cluster, requires the implementation of quantum-mechanics/molecular-mechanics hybrid methods, and will be presented elsewhere [107].

Table 14 (fourth column) shows that the resulting structure of the hydrated Mn_3CaO_4Mn cluster in the high-valent configuration Mn4(IV,IV,III,III), completely ligated with imidazole, carboxylate, chloride, water and hydroxide ions, is very similar to the model of OEC of PSII proposed by the 1S5L X-ray diffraction structure [27], consistent with XAS data [6,87,88,122–125]. In fact, considering that the nuclear geometry of the oxomanganese complex itself remains invisible at the 3.5 Å resolution of the 1S5L structure, it is difficult to judge whether the QM model and the OEC structures are truly identical or whether there are any significant differences. In addition to the moderate resolution, rigorous comparisons to the OEC structure must consider the possible effect of photo-reduction during the process of X-ray data acquisition [87,126].

4. Conclusions

In this paper, we have explored the capabilities and limitations of the DFT/B3LYP methodology as applied to calculations of equilibrium distances, exchange coupling constants and the energetics of low-lying spin-states of mixed-valent multinuclear oxomanganese complexes. We have shown that the hybrid B3LYP functional predicts equilibrium distances and exchange coupling constants of pre-selected spin-electronic states in excellent agreement with X-ray and magnetic data, so long as the μ-oxo bridges are modeled by sufficiently flexible basis sets. It is, therefore, concluded that typical overestimations of Mn–Mn distances by as much as 0.10–0.15 Å, and of Mn–ligand distances along the Jahn–Teller axis of Mn^{3+} ions by as much as 0.23 Å, can be significantly corrected simply by sufficiently expanding the basis set of the ligands coordinated to the Mn ions with polarization functions.

We have shown that the hybrid B3LYP functional erroneously predicts the relative stability of states of different spin multiplicity in the Mn trimer $[Mn_3O_4(bpy)_4(OH_2)_2]^{4+}$. This failure is probably due to the imbalance of exchange and correlation contributions, as found in other transition metal compounds [31,35,39,86]. The re-parameterization of the B3LYP functional to balance such contributions, implemented for other transition metal compounds [31], is found to be insufficient to correct the energetics of low-lying spin states.

Finally, we have shown that the DFT/B3LYP analysis of the hydrated Mn_3O_4CaMn cluster, completely ligated by water, OH^-,Cl^-, carboxylate and imidazole ligands, indicates that the cuboidal model of the inorganic core of the OEC of PSII, proposed by X-ray studies [27], and consistent with XAS [6,87,88,122–125] and EPR [127], is a stable structure even in the absence of ligating amino-acid residues. In addition, its structural and electronic properties are found to be in very good agreement with X-ray data of PSII. These findings suggest that the biomolecular environment surrounding the Mn_3CaO_4Mn cluster of PSII

must conform to the intrinsic structural properties of the inorganic oxomanganese complex in order to position suitable sources and sinks of electrons and protons.

5. Abbreviations

PSII	photosystem II
OEC	O_2-evolving complex
BS	broken symmetry
HS	high spin
EPR	electron paramagnetic resonance
DFT	density functional theory
terpy	2,2′:6,2″-terpyridine
phen	1,10-phenanthroline
bpy	2,2′-bipyridine
L	$Ph_2PO_2^-$
B3LYP	Becke-3–Lee–Yang–Parr
CCDC	Cambridge Crystallographic Data Center
ECPs	electron core potentials
ESP	electrostatic potential

Acknowledgments

V.S.B. acknowledges a generous allocation of supercomputer time from the National Energy Research Scientific Computing (NERSC) center and financial support from Research Corporation, Research Innovation Award #RI0702, a Petroleum Research Fund Award from the American Chemical Society PRF #37789-G6, a junior faculty award from the F. Warren Hellman Family, the National Science Foundation (NSF) Career Program Award CHE #0345984, the NSF Nanoscale Exploratory Research (NER) Award ECS #0404191, the Alfred P. Sloan Fellowship (2005–2006), a Camille Dreyfus Teacher-Scholar Award for 2005, and a Yale Junior Faculty Fellowship in the Natural Sciences (2005–2006). G.W.B acknowledges support from the National Institutes of Health grant GM32715.

References

[1] W.F. Ruettinger, G.C. Dismukes, Chem. Rev. 97 (1997) 1–24.
[2] J. Limburg, J.S. Vrettos, L.M. Liable-Sands, A.L. Rheingold, R.H. Crabtree, G.W. Brudvig, Science 283 (1999) 1524–1527.
[3] Y. Naruta, M. Sasayama, T. Sasaki, Angew. Chem., Int. Ed. 33 (1994) 1839–1841.
[4] R. Manchanda, G.W. Brudvig, S. de Gala, R.H. Crabtree, Inorg. Chem. 33 (1994) 5157–5160.
[5] J.E. Sarneski, H.H. Thorp, G.W. Brudvig, R.H. Crabtree, G. Schulte, J. Am. Chem. Soc. 112 (1990) 7255–7260.
[6] S. Mukhopadhyay, S.K. Mandal, S. Bhaduri, W.H. Armstrong, Chem. Rev. 104 (2004) 3981–4026.
[7] R. Manchanda, G.W. Brudvig, R.H. Crabtree, Coord. Chem. Rev. 144 (1995) 1–38.
[8] R.D. Britt, K.A. Campbell, J.M. Peloquin, M.L. Gilchrist, C.P. Aznar, M.M. Dicus, J. Robblee, J. Messinger, Biochim. Biophys. Acta 1655 (2004) 158–171.
[9] Y. Kimura, K. Hasegawa, T. Yamanari, T. Ono, Photosynth. Res. 84 (2005) 245–250.
[10] T.A. Roelofs, W.C. Liang, M.J. Latimer, R.M. Cinco, A. Rompel, J.C. Andrews, K. Sauer, V.K. Yachandra, M.P. Klein, Proc. Natl. Acad. Sci. USA 93 (1996) 3335–3340.
[11] P.E.M. Siegbahn, R.H. Crabtree, J. Am. Chem. Soc. 121 (1999) 117–127.
[12] P.E.M. Siegbahn, Curr. Opin. Chem. Biol. 6 (2) (2002) 227–235.
[13] P.E.M. Siegbahn, Inorg. Chem. 39 (2000) 2923–2935.
[14] M. Lundberg, P.E.M. Siegbahn, Chem. Phys. Lett. 401 (2005) 347–351.
[15] M. Lundberg, P.E.M. Siegbahn, J. Comput. Chem. 26 (2005) 661–667.
[16] M. Lundberg, R.A.M. Blomberg, P.E.M. Siegbahn, Inorg. Chem. 43 (2004) 264–274.
[17] M. Lundberg, P.E.M. Siegbahn, Phys. Chem. Chem. Phys. 6 (2004) 4772–4780.
[18] S. Petrie, R. Stranger, Inorg. Chem. 43 (2004) 5237–5244.
[19] S. Sinnecker, F. Neese, L. Noodleman, W. Lubitz, J. Am. Chem. Soc. 126 (2004) 2613–2622.
[20] S. Sinnecker, F. Neese, W. Lubitz, J. Biol. Inorg. Chem. 10 (2005) 231–238.
[21] P.E.M. Siegbahn, M.R.A. Blomberg, Biochim. Biophys. Acta 1655 (2004) 45–50.
[22] M. Lundberg, M.R.A. Blomberg, P.E.M. Siegbahn, Theor. Chem. Acc. 110 (2003) 130–143.
[23] M. Lundberg, P.E.M. Siegbahn, J. Phys. Chem. B 109 (2005) 10513–10520.
[24] X.G. Zhao, W.H. Richardson, J.L. Chen, J. Li, L. Noodleman, H.L. Tsai, D.N. Hendrickson, Inorg. Chem. 36 (1999) 1198–1217.
[25] A.D. Becke, J. Chem. Phys. 98 (1993) 1372–1377.
[26] A.D. Becke, J. Chem. Phys. 98 (1993) 5648–5652.
[27] K.N. Ferreira, T.M. Iverson, K. Maghlaoui, J. Barber, S. Iwata, Science 303 (2004) 1831–1838.
[28] J.S. Vrettos, J. Limburg, G.W. Brudvig, Biochim. Biophys. Acta 1503 (2001) 229–245.
[29] V.K. Yachandra, K.S.M.P. Klein, Chem. Rev. 96 (1996) 2927–2950.
[30] W. Koch, M.C.A. Holthausen, in: A Chemist's Guide to Density Functional Theory, Wiley–VCH, Weinheim, 2001.
[31] M. Reiher, O. Salomon, B.A. Hess, Theor. Chem. Acc. 107 (2001) 48–55.
[32] J.N. Harvey, in: T.R. Cundari (Ed.), Computational Organometallic Chemistry, Marcel Dekker, New York, 2001, p. 291.
[33] R. Poli, J.N. Harvey, Chem. Soc. Rev. 32 (2003) 1–8.
[34] J.N. Harvey, R. Poli, K.M. Smith, Coord. Chem. Rev. 238 (2003) 347–361.
[35] O. Salomon, M. Reiher, B.A. Hess, J. Chem. Phys. 117 (2002) 4729–4737.
[36] H. Schwarz, Int. J. Mass Spectrom. 237 (2004) 75–105.
[37] D. Schroder, S. Shaik, H. Schwarz, Acc. Chem. Res. 33 (2000) 139–145.
[38] S. Shaik, S.P. deVisser, F. Ogliaro, H. Schwarz, D. Schroder, Curr. Opin. Chem. Biol. 6 (2002) 556–567.
[39] M.C. Holthausen, J. Comput. Chem. 26 (2005) 1505–1518.
[40] A.E. Mattsson, Science 298 (2002) 759–760.
[41] R. Ahlrichs, F. Furche, S. Grimme, Chem. Phys. Lett. 325 (2000) 317–321.
[42] S. Riedel, M. Straka, M. Kraupp, Phys. Chem. Chem. Phys. 6 (2004) 1122–1127.
[43] V. Guner, K.S. Khuong, A.G. Leach, P.S. Lee, M.D. Bartberger, K.N. Houk, J. Phys. Chem. A 107 (2003) 11445–11459.
[44] H.L. Woodcock, H.F. Schaefer, P.R. Schreiner, J. Phys. Chem. A 107 (2002) 11923–11931.
[45] C. Adamo, V. Barone, J. Chem. Phys. 110 (1999) 6158–6170.
[46] C. Adamo, A. di Mateo, P. Rey, V. Barone, J. Phys. Chem. A 103 (1999) 3481–3488.
[47] C. Adamo, V. Barone, A. Bencini, F. Totti, I. Ciofini, Inorg. Chem. 38 (1999) 1996–2004.

[48] C. Adamo, M. Ernzerhof, G.E. Scuseria, J. Chem. Phys. 112 (2000) 2643–2649.
[49] A.J. Cohen, N.C. Handy, Chem. Phys. Lett. 316 (2000) 155–160.
[50] A.D. Boese, J.M.L. Martini, N.C. Handy, J. Chem. Phys. 119 (2003) 3005–3014.
[51] A.D. Boese, J.M.L. Martini, J. Chem. Phys. 121 (2003) 3405–3416.
[52] Y. Zhao, B.J. Lynch, D.G. Truhlar, Phys. Chem. Chem. Phys. 6 (2004) 673–676.
[53] Y. Zhao, D.G. Truhlar, J. Phys. Chem. A 108 (2004) 6908–6918.
[54] Y. Zhao, D.G. Truhlar, J. Chem. Theor. Comput. 1 (2005) 415–432.
[55] X. Xu, W.A. Goddard, J. Chem. Phys. 121 (2004) 4068–4082.
[56] X. Xu, W.A. Goddard, J. Phys. Chem. A 108 (2004) 8595–8604.
[57] X. Xu, Q.S. Zhang, R.P. Muller, W.A. Goddard, J. Chem. Phys. 122 (2005). Art No. 014105.
[58] J.C. Sancho-Garcia, J. Cornil, J. Chem. Phys. 121 (2004) 3096–3101.
[59] S. Andersson, M. Gruning, J. Phys. Chem. A 108 (2004) 7621–7636.
[60] J. Tao, J.P. Perdew, V.N. Staroverov, G.E. Scuseria, Phys. Rev. lett. 91 (2003). Art. No. 146401.
[61] J.P. Perdew, A. Ruzsinszky, J.M. Tao, V.N. Staroverov, G.E. Scuseria, G.I. Csonka, J. Chem. Phys. 123 (2005). Art. No. 062201.
[62] W. Koch, R. Hertwig, in: N.L. Allinger, T. Clark, J. Gasteiger, P. Kollmann, I.H.F. Schaeffer, P.V.R. Schleyer (Eds.), Encyclopedia of Computational Chemistry, Elsevier, Amsterdam, 1998.
[63] T.V. Russo, R.L. Martin, P.J. Hay, J. Chem. Phys. 101 (1994) 7729–7737.
[64] T.V. Russo, R.L. Martin, P.J. Hay, A.K. Rappe, J. Chem. Phys. 102 (1995) 9315–9321.
[65] S. Yanagisawa, T. Tsuneda, K. Hirao, J. Comput. Chem. 22 (2001) 1995–2009.
[66] S. Yanagisawa, T. Tsuneda, K. Hirao, J. Chem. Phys. 112 (2000) 545–553.
[67] C.W. Bauschlicher, G.L. Gutsev, Theor. Chem. Acc. 108 (2002) 27–30.
[68] G.L Gutsev, M.D. Mochena, P. Jena, C.W. Bauschlicher, H. Partridge, J. Chem. Phys. 121 (2004) 6785–6797.
[69] A. Matveev, M. Staufer, M. Mayer, N. Rosch, Int. J. Quantum Chem. 75 (1999) 863–873.
[70] E.J. Baerends, V. Branchadell, M. Sodupe, Chem. Phys. Lett. 265 (1997) 481–489.
[71] I. Dalmazio, H.A. Duarte, J. Chem. Phys. 115 (2001) 1747–1756.
[72] J. Baker, P. Pulay, J. Comput. Chem. 24 (2003) 1184–1191.
[73] A.V. Mitin, J. Baker, P. Pulay, J. Chem. Phys. 118 (2003) 7775–7782.
[74] M. Swart, A.R. Groenhof, A.W. Ehlers, K. Lammertsma, J. Phys. Chem. A 108 (2004) 5479–5483.
[75] C.Y Ren, H.T. Jeng, C.S. Hsue, Phys. Rev. B 66 (2002). Art. No. 125105.
[76] G.L. Gutsev, L. Andrews, C.W. Bauschlicher, Theor. Chem. Acc. 109 (2003) 298–308.
[77] C.W. Bauschlicher, G.L. Gutsev, Theor. Chem. Acc. 107 (2002) 309–312.
[78] G.L. Gutsev, C.W. Bauschlicher, J. Phys. Chem. A 107 (2003) 4755–4767.
[79] C.J. Barden, J.C. Rienstra-Kiracofe, H.F. Schaefer, J. Chem. Phys. 113 (2000) 690–700.
[80] M. Lundberg, P.E.M. Siegbahn, J. Chem. Phys. 122 (2005). Art. No. 224103.
[81] A. Ghosh, P.R. Taylor, Curr. Opin. Chem. Biol. 7 (2003) 113–124.
[82] A. Ghosh, E. Steene, J. Biol. Inorg. Chem. 6 (2001) 739–752.
[83] A. Ghosh, P.R. Taylor, J. Chem. Theor. Comput. 1 (2005) 597–600.
[84] A. Ghosh, B.J. Persson, P.R. Taylor, J. Biol. Inorg. Chem. 8 (2003) 507–511.
[85] A. Ghosh, E. Tangen, H. Ryeng, P.R. Taylor, Eur. J. Inorg. Chem. 23 (2004) 4555–4560.
[86] G. Frenking, N. Frohlich, Chem. Rev. 100 (2000) 717–774.
[87] H. Dau, P. Liebisch, M. Haumann, Phys. Chem. Chem. Phys. 6 (2004) 4781–4792.
[88] M. Haumann, C. Muller, P. Liebisch, L. Iuzzolino, J. Dittmer, M. Grabolle, T. Neisius, W. Meyer-Klaucke, H. Dau, Biochemistry 4 (2005) 1894–1908.
[89] W.F. Ruettinger, D.M. Ho, G.C. Dismukes, Inorg. Chem. 38 (1999) 1036–1037.
[90] Jaguar 5. 5. Schroedinger, L.L.C., Portland, OR, 1991–2003.
[91] M.J. Frisch, G.W. Trucks, H.B. Schlegel, G.E. Scuseria, M.A. Robb, J.R. Cheeseman, J.A. Montgomery Jr., T. Vreven, K.N. Kudin, J.C. Burant, J.M. Millam, S.S. Iyengar, J. Tomasi, V. Barone, B. Mennucci, M. Cossi, G. Scalmani, N. Rega, G.A. Petersson, H. Nakatsuji, M. Hada, M. Ehara, K. Toyota, R. Fukuda, J. Hasegawa, M. Ishida, T. Nakajima, Y. Honda, O. Kitao, H. Nakai, M. Klene, X. Li, J.E. Knox, H.P. Hratchian, J.B. Cross, C. Adamo, J. Jaramillo, R. Gomperts, R.E. Stratmann, O. Yazyev, A.J. Austin, R. Cammi, C. Pomelli, J.W. Ochterski, P.Y. Ayala, K. Morokuma, G.A. Voth, P. Salvador, J.J. Dannenberg, V.G. Zakrzewski, S. Dapprich, A.D. Daniels, M.C. Strain, O. Farkas, D.K. Malick, A.D. Rabuck, K. Raghavachari, J.B. Foresman, J.V. Ortiz, Q. Cui, A.G. Baboul, S. Clifford, J. Cioslowski, B.B. Stefanov, G. Liu, A. Liashenko, P. Piskorz, I. Komaromi, R.L. Martin, D.J. Fox, T. Keith, M.A. Al-Laham, C.Y. Peng, A. Nanayakkara, M. Challacombe, P.M.W. Gill, B. Johnson, W. Chen, M.W. Wong, C. Gonzalez, J.A. Pople, Gaussian-03, Revision A1, 2003.
[92] E. Ruiz, P. Alemany, S. Alvarez, J. Cano, J. Am. Chem. Soc. 119 (1997) 1297–1303.
[93] P. Christian, G. Rajaraman, A. Harrison, M. Helliwell, J.J.W. McDouall, J. Raftery, R.E.P. Winpenny, J. Chem. Soc., Dalton Trans. 39 (2004) 2550–2555.
[94] G. Vacek, J.K. Perry, J.M. Langlois, Chem. Phys. Lett. 310 (1999) 189–194.
[95] L. Noodleman, D.A. Case, Adv. Inorg. Chem. 38 (1992) 423–470.
[96] L. Noodleman, C.Y. Peng, D.A. Case, J.M. Mouesca, Coord. Chem. Rev. 144 (1995) 199–244.
[97] L. Noodleman, J. Li, X.G. Zhao, W.H. Richardson, Density Functional Methods: Applications in Chemistry and Material Science, Wiley, New York, 1997, pp. 137–164.
[98] E. Ruiz, S. Alvarez, J. Cano, P. Alemany, J. Comput. Chem. 20 (1999) 1391–1400.
[99] H.H. Thorp, G.W. Brudvig, New J. Chem. 15 (1991) 479–490.
[100] R. Weiss, V. Bulach, A. Gold, J. Terner, A.X. Trautwein, J. Biol. Inorg. Chem. 6 (2001) 831–845.
[101] S.R. Cooper, M. Calvin, J. Am. Chem. Soc. 99 (1977) 6623–6630.
[102] S.R. Cooper, G.C. Dismukes, M.P. Klein, M. Calvin, J. Am. Chem. Soc. 100 (1978) 7248–7252.
[103] M. Stebler, A. Ludi, H.B. Bürgi, Inorg. Chem. 25 (1986) 4743–4750.
[104] C.D. Delfs, R. Stranger, Inorg. Chem. 39 (2000) 491–495.
[105] J.E. McGrady, R. Stranger, J. Am. Chem. Soc. 119 (1997) 8512–8520.
[106] J.P. McEvoy, J.A. Gascon, E.M. Sproviero, V.S. Batista, G.W. Brudvig, in: D. Bruce, A. van der Est (Eds.), Photosynthesis: Fundamental Aspects to Global Perspectives, Allen Press, Lawrence, KS, 2005, pp. 278–280.
[107] E.M. Sproviero, J.A. Gascón, J.P. McEvoy, G.W. Brudvig, V.S. Batista, J. Chem. Theor. Comput., submitted.
[108] W.F. Ruettinger, C. Campana, G.C. Dismukes, J. Am. Chem. Soc. 119 (1997) 6670–6671.
[109] W.F. Ruettinger, M. Yagi, K. Wolf, S. Bernasek, G.C. Dismukes, J. Am. Chem. Soc. 122 (2000) 10353–10357.
[110] H. Dau, L. Iuzzolino, J. Dittmer, Biochim. Biophys. Acta 1503 (2001) 24–39.
[111] T.A. Ono, T. Noguchi, Y. Inoue, M. Kusunoki, T. Matsushita, H. Oyanagi, Science 258 (1992) 1335–1337.
[112] V.K. Yachandra, V.J. DeRose, M.J. Latimer, L. Mukerji, K. Sauer, M.P. Klein, Science 260 (1993) 675–679.
[113] U. Bergmann, M.M. Grush, C.R. Horne, P. DeMarois, J.E. Penner-Hahn, C.F. Yocum, D.W. Wright, C.E. Dube, W.H. Armstrong, G. Christou, H.J. Eppley, S.P. Cramer, J. Phys. Chem. B 102 (1998) 8350–8352.

[114] L. Iuzzolino, J. Dittmer, W. Dorner, W. Meyer-Klaucke, H. Dau, Biochemistry 37 (1998) 17112–17119.
[115] J. Messinger, J.H. Robblee, U. Bergmann, C. Fernandez, P. Glatzel, H. Visser, R.M. Cinco, K.L. McFarlane, E. Bellacchio, S.A. Pizarro, S.P. Cramer, K. Sauer, M.P. Klein, V.K. Yachandra, J. Am. Chem. Soc. 123 (2001) 7804–7820.
[116] T. Kuntzleman, C.F. Yocum, Biochemistry 44 (2005) 2129–2142.
[117] M.F. Charlot, A. Boussac, G. Blondin, Biochem. Biophys. Acta 44 (2005) 2129–2142.
[118] R.M. Cinco, K.L.M. Holman, J.H. Robblee, J. Yano, S.A. Pizarro, E. Bellacchio, K. Sauer, V.K. Yachandra, Biochemistry 41 (2002) 12928–12933.
[119] R.M. Cinco, J.H. Robblee, A. Rompel, C. Fernandez, K. Sauer, V.K. Yachandra, M.P. Klein, J. Synchrotron Radiat. 6 (1999) 419–420.
[120] R.M. Cinco, J.H. Robblee, A. Rompel, C. Fernandez, V.K. Yachandra, K. Sauer, M.P. Klein, J. Phys. Chem. B 102 (1998) 8248–8256.
[121] M.J. Latimer, V.J. Derose, I. Mukerji, V.K. Yachandra, K. Sauer, M.P. Klein, Biochemistry 34 (1995) 10898–10909.
[122] H. Dau, P. Liebisch, M. Haumann, Anal. Bioanal. Chem. 376 (2003) 562–583.
[123] W.C. Liang, T.A. Roelofs, R.M. Cinco, A. Rompel, M.J. Latimer, W.O. Yu, K. Sauer, M.P. Klein, V.K. Yachandra, J. Am. Chem. Soc. 122 (2000) 3399–3412.
[124] V.K. Yachandra, Phil. Trans. Roy. Soc. Lond. Ser. B 357 (2002) 1347–1357.
[125] J.H. Robblee, J. Messinger, R.M. Cinco, K.L. McFarlane, C. Fernandez, S.A. Pizarro, K. Sauer, V.K. Yachandra, J. Am. Chem. Soc. 124 (2002) 7459–7471.
[126] J. Yano, J. Kern, K.D. Irrgang, M.J. Latimer, U. Bergmann, P. Glatzel, Y. Pushkar, J. Biesiadka, B. Loll, K. Sauer, J. Messinger, A. Zouni, V.K. Yachandra, Proc. Natl. Acad. Sci. USA 102 (2005) 12047–12052.
[127] J.M. Peloquin, R.D. Britt, Biochim. Biophys. Acta 1503 (2001) 96–111.
[128] K. Sauer, V.K. Yachandra, Biochim. Biophys. Acta 1655 (2004) 140–148.